

Search for sub-eV axion-like resonance states via stimulated quasi-parallel laser collisions with the parameterization including fully asymmetric collisional geometry

Kensuke Homma^{a,1}, Yuri Kirita^{b,1}, Masaki Hashida,^{2,3} Yusuke Hirahara,¹ Shunsuke Inoue,^{2,3} Fumiya Ishibashi,¹ Yoshihide Nakamiya,^{2,4} Liviu Neagu,^{4,5} Akihide Nobuhiro,¹ Takaya Ozaki,¹ Madalin-Mihai Rosu,⁴ Shuji Sakabe,^{2,3} and Ovidiu Tesileanu⁴

(SAPPHIRES collaboration)

¹*Graduate School of Advanced Science and Engineering, Hiroshima University, Kagamiyama, Higashi-Hiroshima 739-8526, Japan*

²*Institute for Chemical Research, Kyoto University Uji, Kyoto 611-0011, Japan*

³*Graduate School of Science, Kyoto University, Sakyouku, Kyoto 606-8502, Japan*

⁴*Extreme Light Infrastructure-Nuclear Physics (ELI-NP)/Horia Hulubei National Institute for R&D in Physics and Nuclear Engineering (IFIN-HH), 30 Reactorului St., P.O. Box MG-6, Bucharest-Magurele, Judetul Ilfov, RO-077125, Romania*

⁵*National Institute for Laser, Plasma and Radiation Physics, 409 Atomistilor PO Box MG-36, 077125, Magurele, Jud. Ilfov, Romania*

(Dated: October 8, 2021)

^a co-first author (corresponding author)

^b co-first author

Abstract

We have searched for axion-like resonance states by colliding optical photons in a focused laser field (creation beam) by adding another laser field (inducing beam) for stimulation of the resonance decays, where frequency-converted signal photons can be created as a result of stimulated photon–photon scattering via exchanges of axion-like resonances. A quasi-parallel collision system (QPS) in such a focused field allows access to the sub-eV mass range of resonance particles. In past searches in QPS, for simplicity, we interpreted the scattering rate based on an analytically calculable symmetric collision geometry in both incident angles and incident energies by partially implementing the asymmetric nature to meet the actual experimental conditions. In this paper, we present new search results based on a complete parameterization including fully asymmetric collisional geometries. In particular, we combined a linearly polarized creation laser and a circularly polarized inducing laser to match the new parameterization. A 0.10-mJ/31-fs Ti:sapphire laser pulse and a 0.20-mJ/9-ns Nd:YAG laser pulse were spatiotemporally synchronized by sharing a common optical axis and focused into the vacuum system. Under a condition in which atomic background processes were completely negligible, no significant scattering signal was observed at the vacuum pressure of 2.6×10^{-5} Pa, thereby providing upper bounds on the coupling–mass relation by assuming exchanges of scalar and pseudoscalar fields at a 95% confidence level in the sub-eV mass range.

I. INTRODUCTION

Spontaneous symmetry breaking is the key concept for understanding the fundamental laws of physics. In particular, when a symmetry is global, the appearance of a massless Nambu–Goldstone boson (NGB) [1] may be expected as a result of the broken symmetry. This viewpoint can be a robust guiding principle for predicting new particle states based on various types of global symmetries in different theoretical contexts, including axion [2], dilaton [3], inflaton [4], and string-inspired models [5]. However, NGBs are observed as pseudo-NGB states (pNGB) with finite masses due to complicated quantum corrections, such as pions in the context of quantum chromodynamics (QCD). If pNGBs are coupled only very weakly to matter, they could be natural candidates to explain the dark components of the universe [6–8]. When pNGB masses are relatively small and the couplings to matter are feeble, they are referred to herein as axion-like particles (ALPs). Although ALP masses are supposed to be small, how small is not known theoretically. Therefore, experimental efforts to search for ALPs over wide low-mass and weak-coupling domains are valuable for discovering some of the dark components of the universe.

The XENON1T experiment recently reported an excess of electron recoil events compared with the defined background level [9]. Among three possible scenarios to explain this excess, the solar axion interpretation is the one that fits most nicely with the recoiled electron energy spectrum with 3.5σ significance. The consistent axion mass range is $\mathcal{O}(0.1\text{--}10)$ eV in the photon–axion coupling range of $\mathcal{O}(10^{-12}\text{--}10^{-9})$ GeV $^{-1}$ depending on the electron–axion coupling and the QCD axion models [10, 11]. However, there is strong tension between this interpretation and the existing constraints from stellar cooling [12–16]. If the aforementioned significance level further increases through improved observations in the near future and the solar axion scenario remains the one that is most valid, then this tension becomes a real issue. To resolve this issue, model-independent observations of the direct production of axions and their decay in laboratory experiments would be indispensable.

In this paper, we focus on the coupling between sub-eV ALPs and laser photons. To describe the coupling of scalar (ϕ) or pseudoscalar (σ) ALPs to two photons, the following two effective Lagrangians are considered:

$$-L_\phi = gM^{-1}\frac{1}{4}F_{\mu\nu}F^{\mu\nu}\phi, \quad -L_\sigma = gM^{-1}\frac{1}{4}F_{\mu\nu}\tilde{F}^{\mu\nu}\sigma, \quad (1)$$

where g is a dimensionless constant for a given energy scale M at which a relevant global

symmetry is broken, and $F^{\mu\nu} = \partial^\mu A^\nu - \partial^\nu A^\mu$ is the electromagnetic field strength tensor and its dual $\tilde{F}^{\mu\nu} \equiv \varepsilon^{\mu\nu\alpha\beta} F_{\alpha\beta}$ with the Levi-Civita symbol ε^{ijkl} .

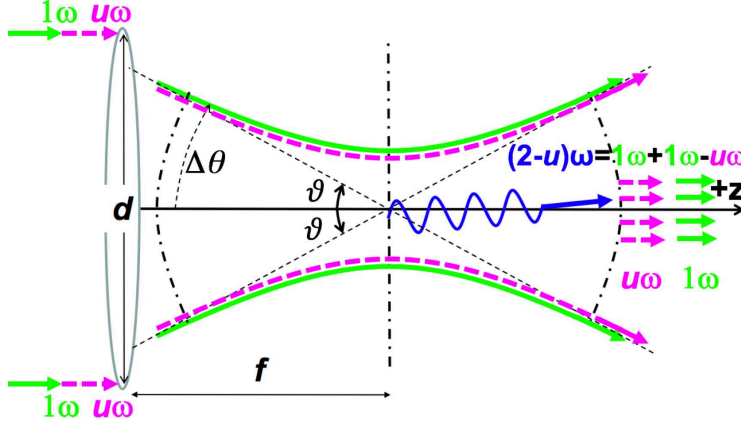


FIG. 1: Concept of stimulated resonant photon–photon scattering in a quasi-parallel collision system (QPS) by focusing two-color laser fields in a vacuum. This figure is quoted from [19] with a slight modification. A coherent field with energy ω (solid green line) is combined with a different-color coherent field with energy $u\omega$ ($0 < u < 1$) (dashed red line). The combined fields are focused by a lens element in a vacuum. Emission of signal photons with energy $(2-u)\omega$ (blue wavy line) is stimulated as a result of energy–momentum conservation in the scattering process $\omega + \omega \rightarrow \phi/\sigma \rightarrow (2-u)\omega + u\omega$ via a resonance state ϕ/σ . Given the focusing parameters of beam diameter d and focal length f , the incident angle ϑ is expected to vary over $0 < \vartheta \leq \Delta\theta$. This unavoidable ambiguity of the wave vectors of the incident light waves provides a wide window for accessing different center-of-mass system energies at a given point in time.

Focusing on sub-eV ALPs, we have proposed to utilize quasi-parallel collision system (QPS) between two photon pairs with equal energy ω by combining and focusing two-color lasers along a common optical axis [17] as illustrated in Fig. 1. The corresponding center-of-mass system (CMS) energy in the QPS is expressed as

$$E_{CMS} = 2\omega \sin \vartheta, \quad (2)$$

where 2ϑ is the relative angle between a pair of incident photons. By controlling the beam diameter (d) and focal length (f) experimentally, the QPS can be sensitive to ALP resonance states with the mass range of $0 < m < 2\omega \sin \Delta\vartheta$, where m is the ALP mass and $\Delta\vartheta$ can be adjusted by the focusing geometry determined with $\Delta\vartheta \sim (d/2)/f$.

The first key feature of the proposed method [17] is the resonant ALP production via the s -channel exchange within the E_{CMS} uncertainty, which drastically enhances the production rate [17]. The second key feature is stimulated decays of produced ALPs to fixed final states via energy–momentum conservation between four photons in the initial and final states. This stimulated resonant scattering rate eventually becomes proportional to the square of the number of photons in the creation laser beam and to the number of photons in the inducing laser beam. This cubic dependence on the number of photons in the beams offers opportunities to search for ALPs with extremely weak coupling when the beam intensity is high enough [18].

In past searches [19–21], we provided constraints on the coupling–mass relation based on a symmetric QPS interpretation in which the incident angles and energies of the two initial-state photons are symmetric (Fig. 1). Based on this parameterization, we provided conservative constraints, and we respected the simple analytic treatment with symmetric collisions because the initial search was made with narrow-bandwidth lasers. However, in a short-pulse laser that is close to the Fourier-transform limit, where the relation between laser frequency and time duration is governed by the wavelike nature of the system (i.e., the uncertainty principle), we must accept an energy spread in principle, and so the approximation of symmetric incident energies is not realistic. In addition, at the diffraction limit where the beam diameters reach their minimum values, the incident angles must also fluctuate greatly because of momentum–position uncertainties. Therefore, we must accept a situation in which the incident photon energies and angles are both asymmetric. Recently, we formulated the interaction rate based on the fully asymmetric collision system [18], where the non-coaxial geometry of the two-photon collisions and stimulated decays are explicitly included with respect to a given coaxial geometry of focused beams (Fig. 2b).

In general, linear polarization states in laser beams are supposed to be fixed precisely. However, linear polarization states around a focal point are not simple plane-wave states because the directions of the wave vectors are not identical in three dimensions, as illustrated in Fig. 3, even if the wave vectors are all aligned to a unique direction before focusing. If we require the transverse wave states of individual light waves, then the polarization directions of individual light waves must fluctuate depending on the individual wave vector directions. Therefore, these fluctuations must be included in both the creation and inducing lasers around the focal points. In order for the stimulation due to the associated inducing field

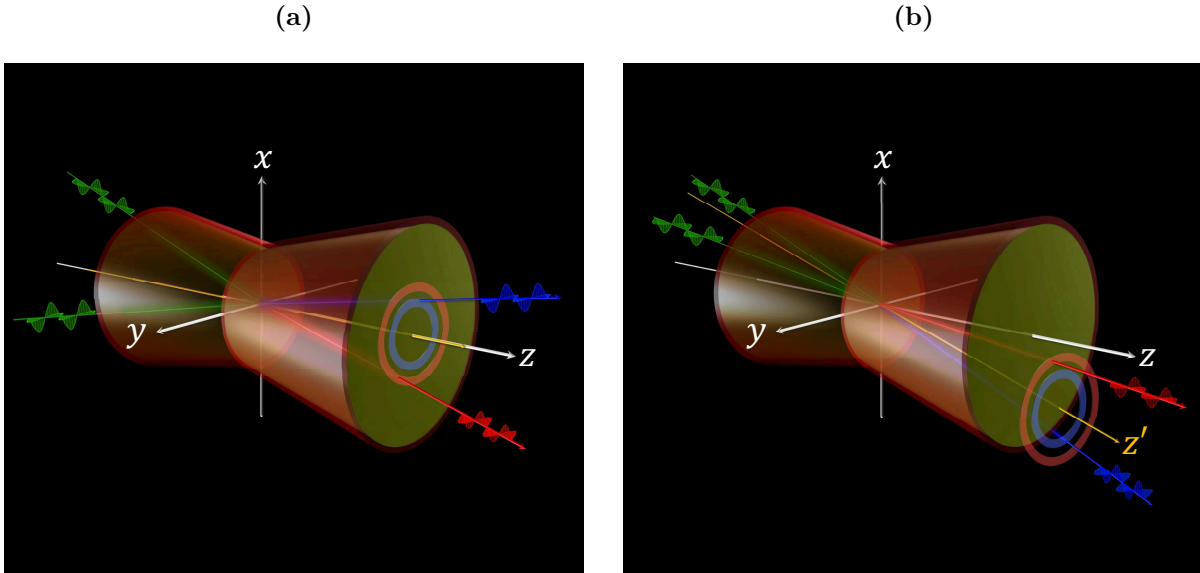


FIG. 2: Classification of collision geometries in QPS. The two figures are extracted from Fig.1 of [18]. (a) Symmetric incidence and coaxial scattering, where the incident angles of the two wave vectors and their energies are symmetric, and the transverse momentum of the photon pair, p_T , always vanishes with respect to the common optical axis z . (b) Asymmetric incidence and non-coaxial scattering, where the incident angles of the two wave vectors and their energies are asymmetric, resulting in a finite value of p_T with respect to the common optical axis z . The zero- p_T axis (z' -axis) is always configurable for arbitrary pairs of incident wave vectors.

to be effective, one of the final-state light waves must coincide with the momentum and also with the linear polarization state of the inducing laser waves. Therefore, fluctuations of linear polarization directions make the evaluation of the stimulation effect in non-coaxial scattering events very complicated because coaxial symmetry of the inducing laser beam is no longer applicable. However, if a collection of light waves is circularly polarized, we can avoid this complication because even if the directions of the waves in three dimensions are changed, the individual light waves retain the circular polarization. Therefore, in [18] we evaluated the stimulation effect based on circularly polarized laser beams. However, there is an experimental constraint in that high-intensity laser pulses are provided as linearly polarized states, and changing their polarization from linear to circular adds a technical difficulty. In this paper, we report new results for sub-eV ALP searches by combining linearly

and circularly polarized states for the creation and inducing lasers, respectively, based on the parameterization including the fully asymmetric collision geometry in QPS. This is in contrast to previous works in which we reported searches based on the symmetric QPS approximation with linear polarization states for both the creation and inducing lasers [19–21].

II. FORMULAE FOR OBTAINING m - g/M RELATION NUMERICALLY IN GENERAL QPS GEOMETRY

Stimulated resonant photon–photon scattering in the most general collisional geometry including asymmetric incidence and non-coaxial scattering was formulated in [18], and the full details can be found in the appendix of [18]. In the following subsections, we briefly explain how to relate the physical parameters of mass m and coupling g/M with the observed number of stimulated photon signals by reviewing only the relevant formulae to discuss the interaction rate dedicated for this search. We specifically replace the vertex factors in the scattering amplitude because we must change from the circular polarization formulated in [18] to the linear one for both scalar and pseudoscalar field exchanges in this search.

We address a search for signal photons p_3 for the following degenerate case in the generic QPS:

$$\langle p_c(p_1) \rangle + \langle p_c(p_2) \rangle \rightarrow p_3 + \langle p_i(p_4) \rangle, \quad (3)$$

where $\langle \ \rangle$ indicates that p_1 and p_2 are chosen stochastically from a single focused coherent beam whose central four-momentum is p_c for the creation of ALPs via s -channel photon–photon scattering, while the focused coherent beam with the central four-momentum p_i is co-moving to induce emission of signal photons p_3 when a fraction of the p_i beam coincides with p_4 .

In symmetric incidence and coaxial scattering as illustrated in Fig. 2a, transverse momenta of stochastically selected wave pairs, p_T , are constraint to be zero with respect to the common optical axis z . Given that the azimuthal angles of the final-state wave vectors are axially symmetric around the z -axis, the evaluation of the inducible momentum or angular range can be greatly simplified owing to the axial symmetric nature of the focused laser beams. In contrast, asymmetric incidence and non-coaxial scattering in Fig. 2b introduces a finite transverse momentum. In this case, a new zero- p_T axis, referred to as the z' -axis,

can be found for the pair of incident wave vectors. Based on the z' -axis, the axial symmetric nature of the azimuthal angles of the final-state wave vectors can be restored. However, the inducing coherent field is still physically fixed to the common optical axis z . This situation complicates the evaluation of the inducible momentum range depending on an arbitrarily formed z' -axis. To solve this complication, a numerical integration is required to express the number of signal photons in the scattering process (3) per pulse collision, \mathcal{Y}_{c+i} , as soon reviewed in the following subsections. With \mathcal{Y}_{c+i} and a set of laser beam parameters P , the number of stimulated signal photons, N_{obs} , as a function of mass m and coupling g/M is eventually expressed as

$$N_{obs} = \mathcal{Y}_{c+i}(m, g/M; P)t_a r \epsilon, \quad (4)$$

where t_a is the data acquisition time, r is the repetition rate of the pulsed beams, and ϵ is the efficiency of detecting p_3 . For a set of m values and an N_{obs} , a set of coupling g/M is evaluated by solving this equation numerically.

A. Induced signal yield \mathcal{Y}_{c+i}

With the average numbers of photons N_c and N_i for the creation and inducing coherent beams, respectively, and units given in [] with units of length L and second s , the induced signal yield \mathcal{Y}_{c+i} per pulse collision is evaluated as

$$\begin{aligned} \mathcal{Y}_{c+i}[1] &= (N_c/2)(N_c/2)N_i \times \\ &\left(\int_{-Z_R/c}^0 dt \int_{-\infty}^{+\infty} d\mathbf{r} \rho_c(\mathbf{r}, t) \rho_c(\mathbf{r}, t) \rho_i(\mathbf{r}, t) V_i \right) \times \\ &\left(\int dQ_I W(Q_I) \frac{c}{2\omega_1 2\omega_2} |\mathcal{M}_s(Q')|^2 dL'_{ips} \right) \\ &\equiv \frac{1}{4} N_c^2 N_i \mathcal{D}_I [s/L^3] \bar{\Sigma}_I [L^3/s]. \end{aligned} \quad (5)$$

\mathcal{D}_I in Eq.(5) is a spatiotemporal overlapping factor in laboratory coordinates (see x, y, z in Fig. 3) of the focused creation beam (subscript c) with the co-moving focused inducing beam (subscript i) limited in the Rayleigh length Z_R only around the focal spot for a conservative evaluation. The following photon number densities $\rho_{k=c,i}$ based on the Gaussian beam

parameterization are integrated over spacetime (t, \mathbf{r}) :

$$\rho_k(t, \mathbf{r}) = \left(\frac{2}{\pi}\right)^{\frac{3}{2}} \frac{1}{w_k^2(ct)c\tau_k} \times \exp\left(-2\frac{x^2 + y^2}{w_k^2(ct)}\right) \exp\left(-2\left(\frac{z - ct}{c\tau_k}\right)^2\right), \quad (6)$$

where w_k are the beam radii as a function of time t whose origin is set at the moment when all the pulses reach the focal point, and τ_k are the time durations of the pulsed laser beams with the speed of light c and the volume of the inducing beam V_i defined as

$$V_i = (\pi/2)^{3/2} w_{i0}^2 c\tau_i, \quad (7)$$

where w_{i0} is the beam waist (minimum radius) of the inducing beam. The actually used overlapping factor configured for the case of different beam diameters between creation and inducing lasers is summarized in the appendix of this paper.

$\bar{\Sigma}_I$ in Eq.(5) is an integrated inducible volume-wise interaction rate that integrates the square of the scattering amplitude $|\mathcal{M}_s(Q')|^2$ over an inducible variable set comprising energies ω_i , polar angles Θ_i , and azimuthal angles Φ_i in laboratory coordinates for $i = 1, 2, 4$: $Q_I \equiv \{Q, \omega_4, \Theta_4, \Phi_4\}$ with $Q \equiv \{\omega_1, \Theta_1, \Phi_1, \omega_2, \Theta_2, \Phi_2\}$ by weighting with multiple Gaussian distributions:

$$W(Q_I) \equiv \Pi_i G_E(\omega_i) G_p(\Theta_i, \Phi_i) \quad (8)$$

with Gaussian distributions on energy G_E and momentum G_p , and also over an inducible Lorentz-invariant phase space in zero- p_T coordinates:

$$dL_{ips}^{\prime I} = (2\pi)^4 \delta(p'_3 + p'_4 - p'_1 - p'_2) \frac{d^3 p'_3}{2\omega_3(2\pi)^3} \frac{d^3 p'_4}{2\omega_4(2\pi)^3} \quad (9)$$

with two incident energies ω_1 and ω_2 , where the primed variables are converted from Q in laboratory coordinates to Q' in zero- p_T coordinates via coordinate rotation. The inducing weight $W(Q_I)$ takes care of the energy and momentum fractions of p_4 satisfying energy-momentum conservation with respect to the energy and momentum distributions of the given inducing laser beam in laboratory coordinates. The essential element of $\bar{\Sigma}_I$ is the Lorentz-invariant scattering amplitude defined in zero- p_T coordinates, $\mathcal{M}_S(Q')$, for the given polarization states $S = abcd$ in a two-body interaction: $p'_1\{a\} + p'_2\{b\} \rightarrow p'_3\{c\} + p'_4\{d\}$. Unless confusion is expected, for simplicity, we omit the prime symbol associated with the momentum vectors in the following explanations.

B. Vertex factors in scattering amplitude \mathcal{M}_S

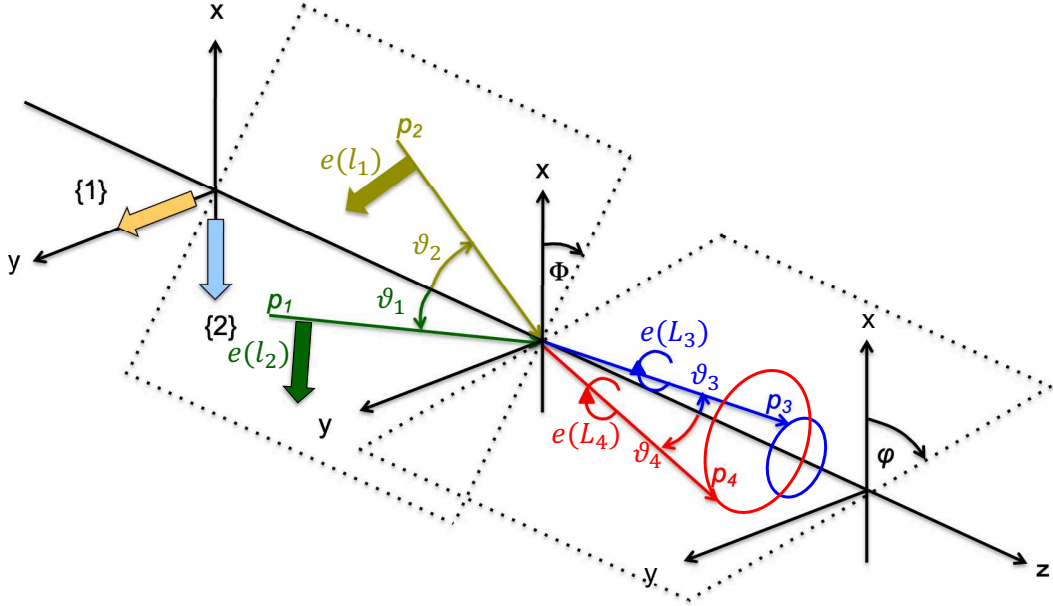


FIG. 3: Definitions of four-momentum vectors p_i and four-polarization vectors $e(\lambda_{p_i})$ with polarization states λ_{p_i} for the initial-state ($i = 1, 2$) and final-state ($i = 3, 4$) light waves. l_i indicates mixture of experimentally defined orthogonal linear polarization states $\{1\}$ and $\{2\}$ before focusing in laboratory coordinates, and L_i indicates left-handed circular polarization states. These polarization vectors are mapped on the rotating reaction planes in the case of asymmetric incident angles and energies in QPS, where the transverse momentum p_T of the $p_1 + p_2$ pair is constraint to be zero as a specially simple case of general asymmetric collisions.

The polarization information is normally useful for distinguishing whether ALPs are scalar or pseudoscalar fields. When a two-body photon-photon scattering process $p_1 + p_2 \rightarrow p_3 + p_4$ in four-momentum space occurs on an identical reaction plane, namely, when the coplanar condition ($\Phi = \varphi = 0$ in Fig. 3) is satisfied, the difference between scalar and pseudoscalar cases becomes distinct. Given an orthogonal set of linear polarization states $\{1\}$ and $\{2\}$, the non-zero scattering amplitudes are limited to the following cases:

$$\begin{aligned}
 p_1\{1\} + p_2\{1\} &\rightarrow p_3\{2\} + p_4\{2\}, \\
 p_1\{1\} + p_2\{1\} &\rightarrow p_3\{1\} + p_4\{1\}
 \end{aligned}
 \tag{10}$$

for scalar field exchange and

$$\begin{aligned}
p_1\{1\} + p_2\{2\} &\rightarrow p_3\{1\} + p_4\{2\}, \\
p_1\{1\} + p_2\{2\} &\rightarrow p_3\{2\} + p_4\{1\}
\end{aligned}
\tag{11}$$

for pseudoscalar field exchange, where swapping $\{1\}$ and $\{2\}$ gives the same scattering amplitudes.

However, as illustrated in Fig. 3, the coplanar condition is, in most cases, not satisfied in QPS in contrast to CMS because the $\vec{p}_1 - \vec{p}_2$ plane and the $\vec{p}_3 - \vec{p}_4$ plane may differ from the x - z plane defined with the laboratory coordinates. Therefore, we must introduce combinations of linear polarization states, l_1 and l_2 , based on the theoretically introduced planes with respect to the experimental linear polarization states $\{1\}$ and $\{2\}$, which are mapped to the y and x axes, respectively. In the following search, we assign the P-polarized state of the creation laser to the $\{2\}$ -state and combine it with the circularly polarized inducing laser. Note here that due to the rotating nature of the incident reaction plane in the focused geometry, even if the experimentally prepared linear polarization state is limited to $\{2\}$, polarization states defined on individual $\vec{p}_1 - \vec{p}_2$ planes can contain both $\{1\}$ and $\{2\}$ components with different projection weights, resulting in sensitivities to both scalar and pseudoscalar fields. This situation is implemented quantitatively in the vertex factors as follows.

Based on expansion of the electromagnetic field strength tensor $F^{\mu\nu}$ and its dual $\tilde{F}^{\mu\nu}$, momentum-polarization tensors corresponding to the expanded coefficients are defined (see Eqs. (A.5) and (A.6) in [18] for details). With a polarization four-vector $e_i(\lambda_p)$ with an arbitrary polarization state λ_p associated with a four-momentum p , and the symbol $*$ indicating the complex conjugate, the momentum-polarization tensors are defined as

$$\begin{aligned}
P^{\mu\nu}(\lambda_p) &\equiv p^\mu e^\nu(\lambda_p) - e^\mu(\lambda_p) p^\nu, \\
\hat{P}^{\mu\nu}(\lambda_p) &\equiv e^{*\mu}(\lambda_p) p^\nu - p^\mu e^{*\nu}(\lambda_p)
\end{aligned}
\tag{12}$$

for the tensor $F^{\mu\nu}$ and

$$\begin{aligned}
\tilde{P}^{\mu\nu}(\lambda_p) &\equiv \varepsilon^{\mu\nu\alpha\beta} (p_\alpha e_\beta(\lambda_p) - e_\alpha(\lambda_p) p_\beta), \\
\hat{\tilde{P}}^{\mu\nu}(\lambda_p) &\equiv \varepsilon^{\mu\nu\alpha\beta} (p_\alpha e_\beta^*(\lambda_p) - e_\alpha^*(\lambda_p) p_\beta)
\end{aligned}
\tag{13}$$

for the dual tensor $\tilde{F}^{\mu\nu}$.

Given the vector and tensor definitions above, the Lorentz-invariant scattering amplitude \mathcal{M}_S dedicated for scalar field exchange is expressed as (see Eq. (A.33) in [18] for the detailed derivation)

$$\mathcal{M}_S = \frac{1}{4} \left(\frac{g}{M} \right)^2 \frac{(P_1 P_2)(\hat{P}_3 \hat{P}_4)}{m^2 - (p_1 + p_2)^2}, \quad (14)$$

where the factors $(P_i P_j)$ in the numerator correspond to the vertex factors reflecting polarization states in the initial and final states, respectively. (ST) is the abbreviation for a momentum-polarization tensor product such as $(ST) \equiv S_{\mu\nu} T^{\mu\nu}$ for four-momenta s and t , that is, $(P_1 P_2)$ corresponds to a momentum-tensor product for four-momenta p_1 and p_2 . In the case of pseudoscalar exchange, we have only to replace the vertex factors with $(P_1 \tilde{P}_2)(\hat{P}_3 \hat{\tilde{P}}_4)$ using Eq. (13).

Hence, necessary momentum-polarization tensor products between four-momenta s and t with their polarization states λ_s and λ_t are summarized as

$$\begin{aligned} S_{\mu\nu}(\lambda_s) T^{\mu\nu}(\lambda_t) &= 2\{(s \cdot t)(e(\lambda_s) \cdot e(\lambda_t)) - (s \cdot e(\lambda_t))(t \cdot e(\lambda_s))\}, \\ \hat{S}_{\mu\nu}(\lambda_s) \hat{T}^{\mu\nu}(\lambda_t) &= 2\{(s \cdot t)(e^*(\lambda_s) \cdot e^*(\lambda_t)) - (s \cdot e^*(\lambda_t))(t \cdot e^*(\lambda_s))\} \end{aligned} \quad (15)$$

for scalar field exchange and

$$\begin{aligned} S_{\mu\nu}(\lambda_s) \tilde{T}^{\mu\nu}(\lambda_t) &= 4\varepsilon^{\mu\nu\alpha\beta} s_\mu e_\nu(\lambda_s) t_\alpha e_\beta(\lambda_t), \\ \hat{S}_{\mu\nu}(\lambda_s) \hat{\tilde{T}}^{\mu\nu}(\lambda_t) &= 4\varepsilon^{\mu\nu\alpha\beta} s_\mu e_\nu^*(\lambda_s) t_\alpha e_\beta^*(\lambda_t) \end{aligned} \quad (16)$$

for pseudoscalar exchange.

The actually used vertex factors for scalar and pseudoscalar field exchanges dedicated for this search with the fixed left-handed circular polarization state, L , of the inducing laser are expressed as follows:

$$\begin{aligned} \text{scalar type} &: (P_1(l_1) P_2(l_2))(\hat{P}_3(L_3) \hat{P}_4(L_4)); \\ \text{pseudoscalar type} &: (P_1(l_1) \tilde{P}_2(l_2))(\hat{P}_3(L_3) \hat{\tilde{P}}_4(L_4)), \end{aligned} \quad (17)$$

where l_i with $i = 1, 2$ represents mixing of linear polarization states $\{1\}$ and $\{2\}$ due to rotation of the $p_1 - p_2$ reaction plane with respect to the linear polarization direction of the creation laser beam, while rotation of the $p_3 - p_4$ reaction plane does not affect the circular polarization states of photons due to helicity conservation. We address only the L -state for p_3 (L_3) induced by the L -state for p_4 (L_4) in the inducing field. This is because vertex

factors combining opposite circular polarization states always vanish, counter-intuitively, in both scalar and pseudoscalar exchanges based on Eqs. (15) and (16).

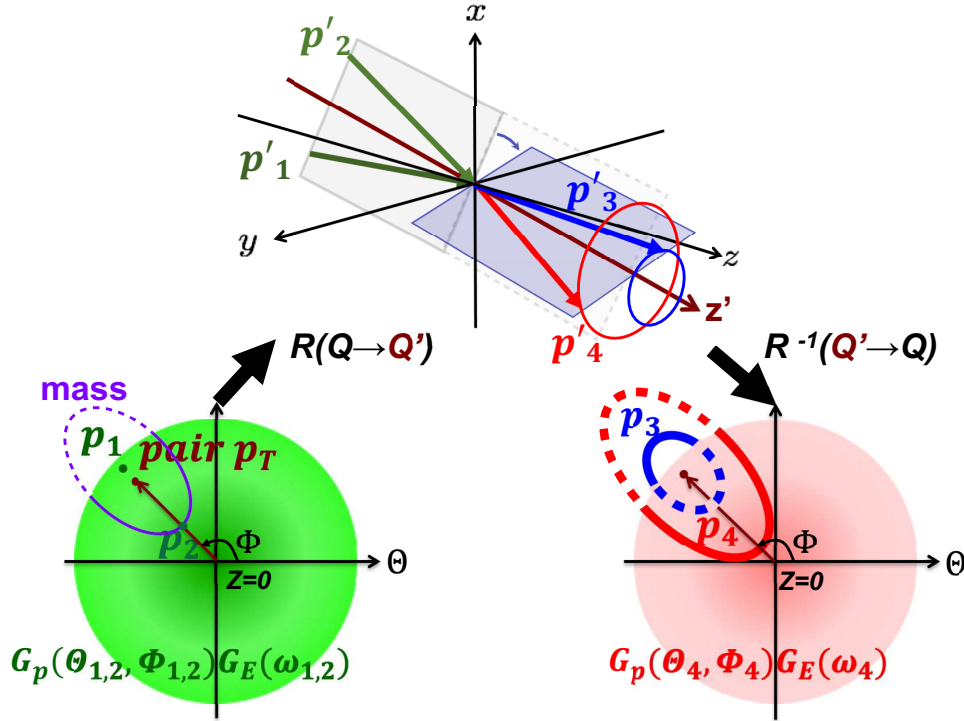


FIG. 4: Flow of numerical calculations. The details are explained in the main text.

C. Outline of numerical calculations

Figure 3 is a special example of an energy-incident-angle asymmetric collision that accidentally shares the common optical axis of the two laser beams, namely, the incident p_T is set to zero. The actual procedures in the numerical calculation including fully asymmetric collisions are explained below based on the illustration in Fig. 4. We first introduce momentum distributions G_p as a function of polar angles Θ_i and azimuthal angles Φ_i mapped on the laboratory coordinates and energy distributions $G_E(\omega_i)$ for the creation (left, green) and inducing (right, red) lasers for individual photons $i = 1, 2, 4$ by denoting G representing normalized Gaussian distributions. Angular distributions in cylindrical coordinates $(\Theta, \Phi, z = 0)$ (diameter corresponds to Θ) are used here representing G_p by fixing momentum norms at energies chosen from G_E . The concrete steps are then as follows. Step 0: Select a finite-size segment of p_1 based on the $G_E(\omega_1)G_p(\Theta_1, \Phi_1)$ distributions. Step 1: A z' -axis of

zero- p_T coordinates is defined by finding a pairing p_2 that satisfies the resonance condition with respect to the selected p_1 and to a finite energy segment from $G_E(\omega_2)$ for a given mass parameter m . The kinematically possible ellipsoidal orbit is drawn with the purple belt on the angular distribution. Step 2: Convert the polarization vectors $e_i(\lambda_i)(i = 1, 2)$ from laboratory coordinates to zero- p_T coordinates through coordinate rotation $R(Q \rightarrow Q')$. Step 3: Calculate the invariant amplitude based on the vertex factors for scalar and pseudoscalar exchanges, respectively, in the given zero- p_T coordinates where the axial symmetric nature of the final-state p'_3 and p'_4 around z' is preserved. Step 4: To evaluate the inducing effect with respect to $G_E(\omega_4)G_p(\Theta_4, \Phi_4)$ defined in laboratory coordinates, a matching fraction of p_4 is calculated after rotating back to the laboratory coordinates from the zero- p_T coordinates, denoted by $R^{-1}(Q' \rightarrow Q)$. Based on the spread of $G_E(\omega_4)$, the red ellipsoidal belt is determined via energy-momentum conservation. Note here that due to the circular polarization state of the inducing beam, any p_4 experiencing scattering can satisfy the polarization matching to the p_i beam. Step 5: p_3 must balance with p_4 through energy-momentum conservation, so we can define a parametric signal energy spread via $\omega_s \equiv \omega_3 = \omega_1 + \omega_2 - \omega_4$ as well as the polar and azimuthal angle spreads by taking the $G_E(\omega_4)G_p(\Theta_4, \Phi_4)$ distribution into account. The volume-wise interaction rate $\bar{\Sigma}_I$ is integrated over the inducible solid angle of p_3 calculated from all the energy and angular spreads. Step 6: The signal yield \mathcal{Y}_{c+i} is finally calculated based on Eq. (5).

III. EXPERIMENTAL SETUP

Figure 5 illustrates the searching setup. A linearly polarized creation beam (Ti:sapphire pulsed laser) and a circularly polarized inducing beam (Nd:YAG pulsed laser) were combined with a dichroic mirror (DM2) in the transport chamber by sharing a common optical axis. At P1 in advance of the pulse compression, the linear polarization state of the creation laser was introduced. To transmit only P-polarized waves, P1 was made of 30 synthetic quartz plates tilted at Brewster's angle. The measured extinction ratio with the full energy shots was approximately 1000 (P-pol.) : 1 (S-pol.). The inducing laser was initially produced at P2 as a linearly polarized beam with a commercial polarization beam splitter with an extinction ratio of 200 (P-pol.) : 1 (S-pol.), and then the linear polarized state was further converted into the circular polarization state by a quarter-plate ($\lambda/4$).

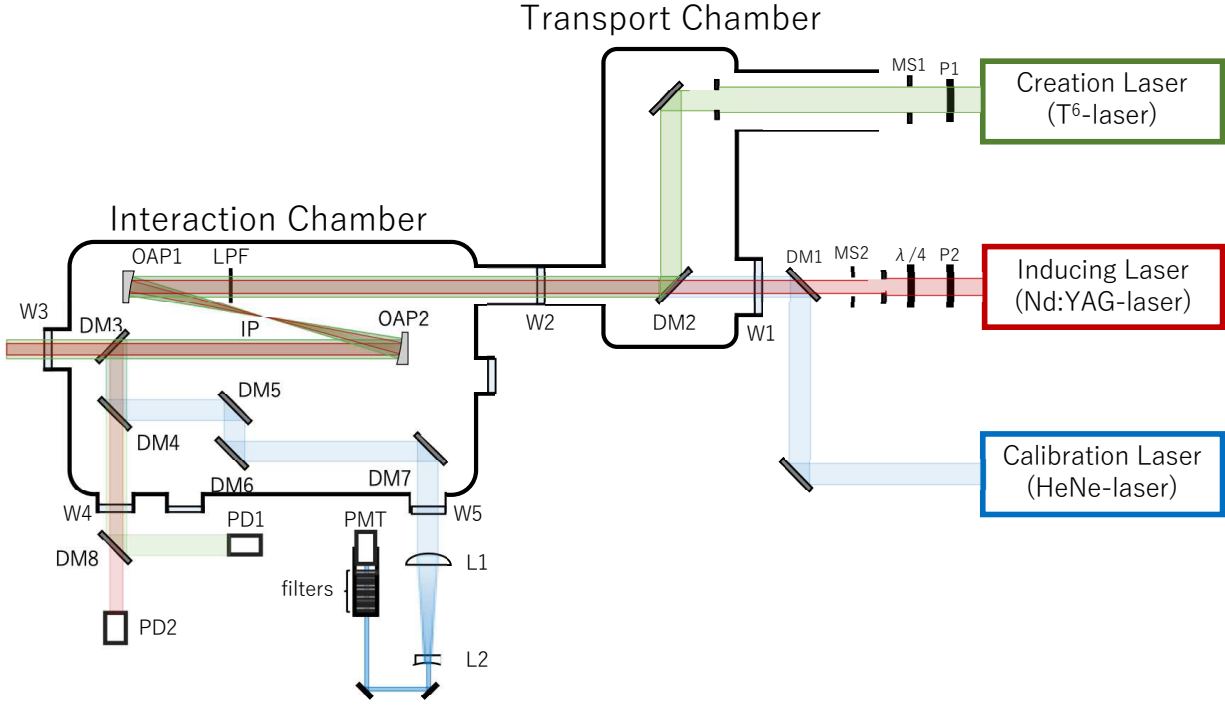


FIG. 5: Schematic of the searching system contained in the beam transport chamber and interaction chamber designed to achieve 10^{-8} Pa.

The central wavelengths of the creation and inducing lasers were 816 and 1064 nm, respectively, their pulse durations were 31 fs and 9 ns, respectively, and their beam diameters were 37 and 16 mm, respectively. Inside the interaction chamber, the two incident beams were focused simultaneously in the vacuum by an off-axis parabolic mirror (OAP1) with a focal length of 279.1 mm. Based on an infinity-corrected optical system, focal-spot images of the two beams were transferred to a CCD camera outside the interaction chamber. The camera recorded the number of beam photons per pixel with a spatial resolution of $0.3 \mu\text{m}$. A thin mesh with a known physical size located at the interaction point (IP) was used to calibrate the physical image size on the CCD camera. By adjusting optical components inside the transport chamber for the creation laser and ones outside the chamber for the inducing laser, spatial overlap was ensured based on the focal spot images of the two beams. The symmetrically placed identical off-axis parabolic mirror (OAP2) located at the point subtending the IP collected the signal waves by restoring the plane-wave propagation of the two incident beams. The intense incident beams were dumped through a dichroic mirror

(DM3) that allowed the two incident beams to pass through while reflecting the signal waves.

With respect to the central wavelengths λ_c and λ_i for the creation and inducing lasers, respectively, the central wavelength λ_s of the signal is defined by $\lambda_s = (2/\lambda_c - 1/\lambda_i)^{-1} = 651$ nm. This wavelength is close to the 633 nm of a He:Ne laser, so a He:Ne laser was combined at DM1 and DM2 with the inducing and creation lasers, respectively, as a calibration source, by which one can trace the signal trajectory down to the signal detector. This calibration laser was used for aligning all the optical components inside the interaction chamber, and it also had a role in evaluating the acceptance factor from the IP to the detector with the specified circular polarization state.

The dichroic mirrors DM3–DM7 were custom-made and commonly reflected 651 nm with 99% while transmitting around 816 nm with 99% and 1064 nm with 95%, to pick up the signal waves among the residual creation and inducing laser beams. To provide timing signals to synchronize the creation and inducing pulses and also to monitor the stability of the pulse energies, photodiodes (PD1, PD2) with a time resolution of ~ 40 ps were used by sampling the attenuated combined pulses that had passed through DM4.

A signal detector was used in the form of an R7400-01 single-photon-countable photomultiplier tube (PMT) manufactured by HAMAMATSU. The falling time resolution was 0.75 ns, which is close to the waveform sampling resolution of 0.5 ns as explained below. For the signal wavelengths of 610–690 nm to be selected, a set of a low-pass filters transmitting above 610 nm and three types of band-pass filters transmitting 570–800 nm, 500–930 nm, and 450–690 nm were installed in front of the PMT to remove residual photons from the intense incident lasers.

The voltages from the PMT and the two PDs as functions of time were recorded using a waveform digitizer with a time resolution of 0.5 ns. The digitizer was triggered by a basic 10-Hz laser oscillator clock to which the incident timing between the creation and inducing lasers was synchronized. The incident rate of the creation laser was reduced to equi-interval 5 Hz by a mechanical shutter (MS1), whereas that of the inducing laser was adjusted to non-equi-interval 5 Hz by a mechanical shutter (MS2) to produce four staggered trigger patterns for the offline waveform analysis. The four types of trigger were as follows: (i) two-beam incidence, “S”; (ii) only inducing-laser incidence, “I”; (iii) only creation-laser incidence, “C”; (iv) no beam incidence, “P”. These were issued in order over a data acquisition run, which ensured equal shot statistics per trigger pattern and also minimized the systematic

uncertainties associated with subtractions between trigger patterns as explained in the next section.

IV. DATA ANALYSIS

A. Counting number of photons by means of a peak finder

The number of photons was evaluated based on the digitized waveform data from the PMT. In a waveform (sometimes referred to as a shot), voltage values V_i were recorded with respect to individual sampling point i within a 500-ns time interval as shown in Fig. 6. Because the time resolution (i.e., the width of a time bin) is 0.5 ns, i runs from 1 to 1000. A peak finder identifies peak structures in a waveform on a shot-by-shot basis and counts the number of observed photons by the following steps: (i) the finder determines an average voltage V_0 over $i = 1$ to 400; (ii) by setting a proper threshold voltage V_{th} , the finder identifies a minimum voltage V_m at $i = m$ in the peak-like domain above V_{th} ; (iii) a half-voltage value is defined as $V_{half} = (V_m + V_0)/2$; (iv) along the forward (f) and backward (b) directions in time, the finder determines time points $i = f$ and $i = b$ at which voltage values exceed V_{half} ; (v) from $i = f, b$, the falling ($i = l$) and rising ($i = u$) edges of a peak are defined as $l = m - (2(m - b) - 1)$ and $u = m + 2(f - m)$, respectively; (vi) a charge sum Q contained in the peak-like structure depicted as the shaded area in Fig. 6 is evaluated as $Q = \sum_{i=l}^u V_i \Delta t / R$ with $\Delta t = 0.5$ ns and $R = 50 \Omega$; (vii) given a single-photon equivalent charge $Q_{p.e.} = (8.206 \pm 0.015) \times 10^{-14}$ C calibrated in advance, $Q/Q_{p.e.}$ provides the observed number of photons in the peak-like structure.

B. Pressure dependence of atomic four-wave mixing process

Nonlinear optical parametric effects caused by third-order polarization susceptibility $\chi^{(3)}$, so-called four-wave mixing (FWM) [22], are expected to occur even in the residual gas in the interaction vacuum chamber. This can be a dominant background source because the wavelengths generated in atomic FWM are nearly equal to those of stimulated scattering in a vacuum due to the kinematic similarity based on energy–momentum conservation between the initial and final state photons. Therefore, we can refer to the searched-for stimulated scattering process as FWM in a vacuum. Meanwhile, atomic FWM is quite useful for

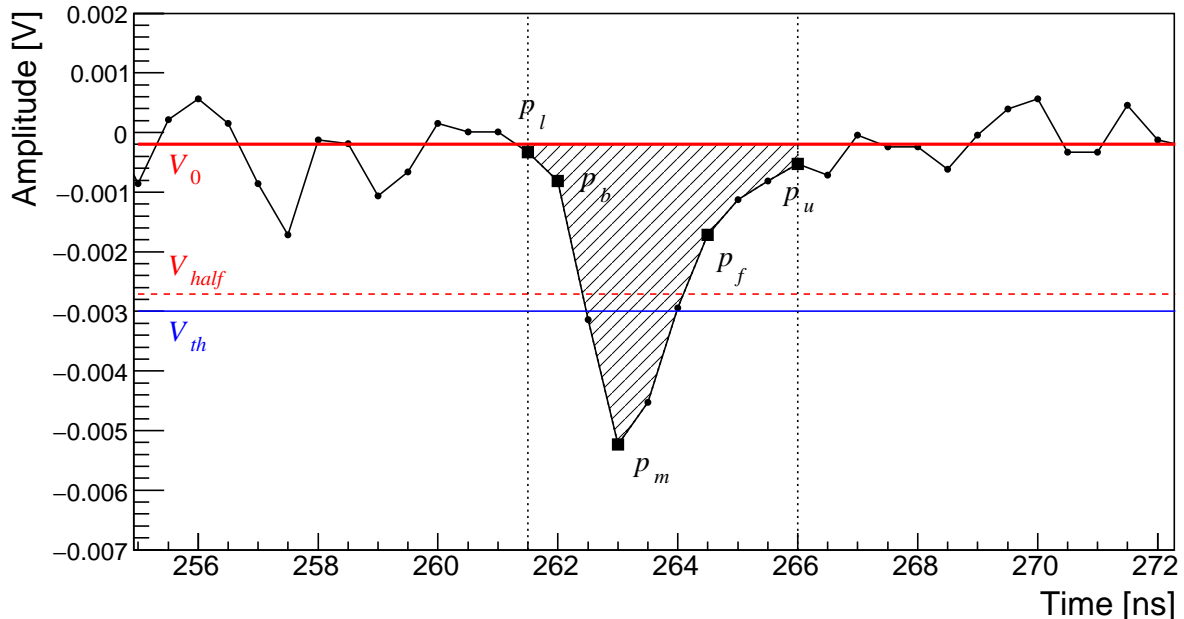


FIG. 6: Waveform sample including a peak with a single trigger. The shaded area shows the integral range used to evaluate the charge sum of the peak structure.

ensuring spatiotemporal synchronization between the creation and inducing pulse lasers in QPS. To validate our searching system, we measured the pressure dependence of the number of atomic FWM photons. Because the peak finder can provide the falling edges of photon incident peaks in the waveforms, the arrival-time distribution as shown in Fig. 7 is measurable in units of the number of photons for each of the four trigger patterns. This figure shows the results measured at 10 Pa. The peak structures appeared in trigger patterns S and C. The peak seen in pattern C is expected because of plasma creation at the IP because the creation laser intensity is high enough to induce ionization of residual atoms. In contrast, the intensity of the inducing laser field is much lower because of the long time duration, as seen in pattern I where no peak is found. Meanwhile, the higher peak seen in pattern S is expected to be the sum between the atomic FWM and the plasma-origin photon yields.

The basic assumption that addition of the number of photons in individual trigger patterns corresponds to the number of photons in trigger pattern S is indeed supported by the following subtraction analysis. The acceptance-uncorrected number of atomic FWM photons, N_S , can be obtained via

$$N_S = (n_S - n_P) - (n_C - n_P) - (n_I - n_P) = n_S - n_C - n_I + n_P, \quad (18)$$

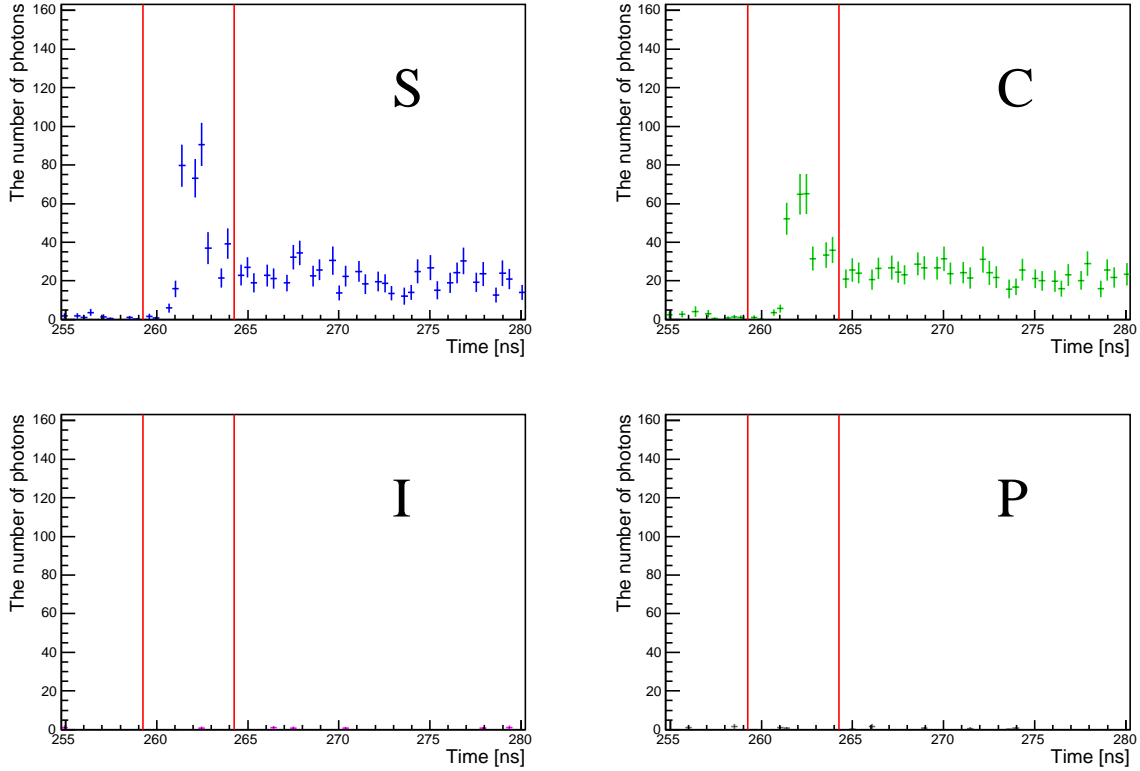


FIG. 7: Arrival-time distributions of number of observed photons by combining the P-polarization state (creation) and the left-handed circular polarization state (inducing) for individual trigger patterns at 10 Pa. The individual time windows in which signal photons are expected to be detected are indicated with the two red lines.

where n_i is the number of photons for trigger pattern i measured in the time interval subtended by the two red vertical lines corresponding to the signal generation timing window. Figure 8 shows the pressure dependence of the number of signal photons per shot, which is expected to be dependent upon the square of the pressure because the photon yield of the atomic FWM should be proportional to $(\chi^{(3)})^2 \propto (\text{density})^2 \propto (\text{pressure})^2$. The dependence was thus fitted with

$$N_S/\text{shot} = a\mathcal{P}^b, \quad (19)$$

where a and b are fitting parameters and \mathcal{P} is pressure. The error bars are the quadratic sum of the statistical error propagation associated with the subtraction process between trigger patterns and systematic uncertainties of focal-point stability during a run period. We explain these uncertainties in the following subsection. As expected, $b = 1.85 \pm 0.35$ is

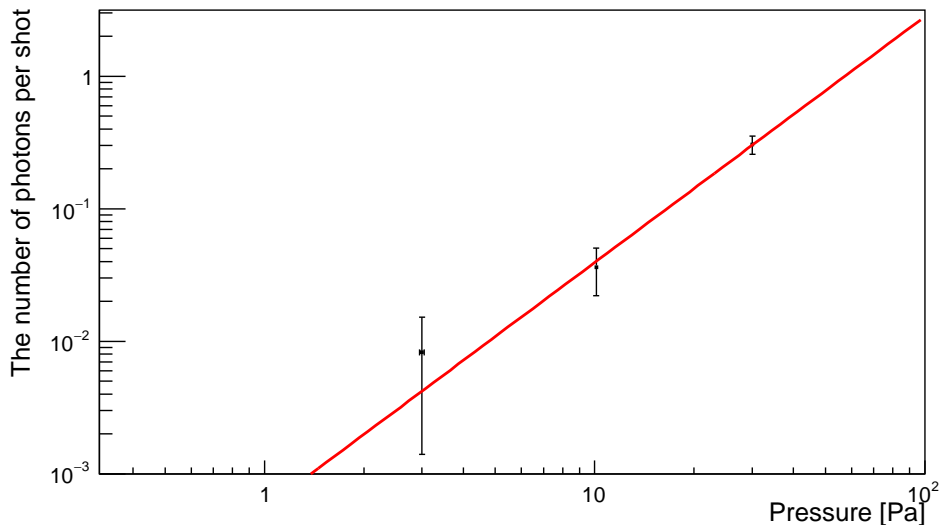


FIG. 8: Pressure dependence of number of four-wave-mixing photons per shot from residual atoms inside interaction chamber when P-pol. (creation) and left-handed circular (inducing) polarization laser pulses are combined and focused.

close to the expected behavior $N_S \propto \mathcal{P}^2$ in atomic physics [20, 22]. Note that this pressure dependence itself is valuable as data because the special combination between linear and circular polarization state beams is a very rare case in atomic physics.

C. Focal-point stability

The systematic uncertainties due to focal-point fluctuations were estimated from overlaps between the two laser focal-spot profiles measured by the common CCD camera sensitive to both wavelengths. Figure 9 shows typical focal-spot images of the creation and inducing lasers.

With the local intensity per CCD pixel of the monitor camera, $N(x, y)$, the overlap factor O is defined as

$$O \equiv \sum_x^c \sum_y^c N_c^2(x, y) N_i(x, y), \quad (20)$$

where the subscripts c and i specify the creation and inducing lasers, respectively. The summations were taken over the area framed by the full width at half maximum of the creation laser intensity profile. Fluctuations of the overlap factors with respect to the mean

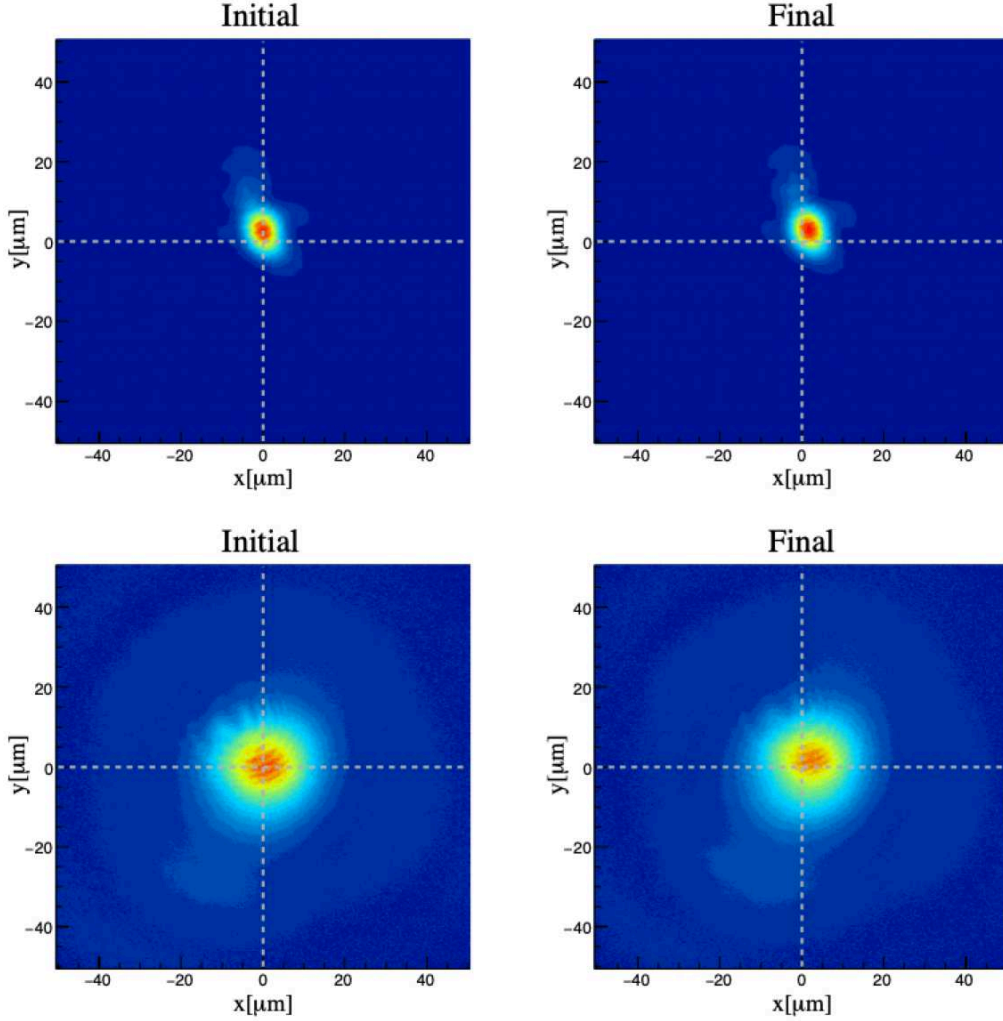


FIG. 9: Beam profiles of creation (upper) and inducing (lower) lasers at interaction point as captured by a common CCD camera. The left and right figures correspond to typical images taken at the beginning and end of a unit run period, where slight deviations in the focal spots are seen.

overlap factor $(O_I + O_F)/2$ were then evaluated as

$$\delta N_S = \left| N_S \frac{O_I - O_F}{O_I + O_F} \right|, \quad (21)$$

where $O_{I,F}$ are the overlap factors at the beginning and end, respectively, of a 2000-s unit run period.

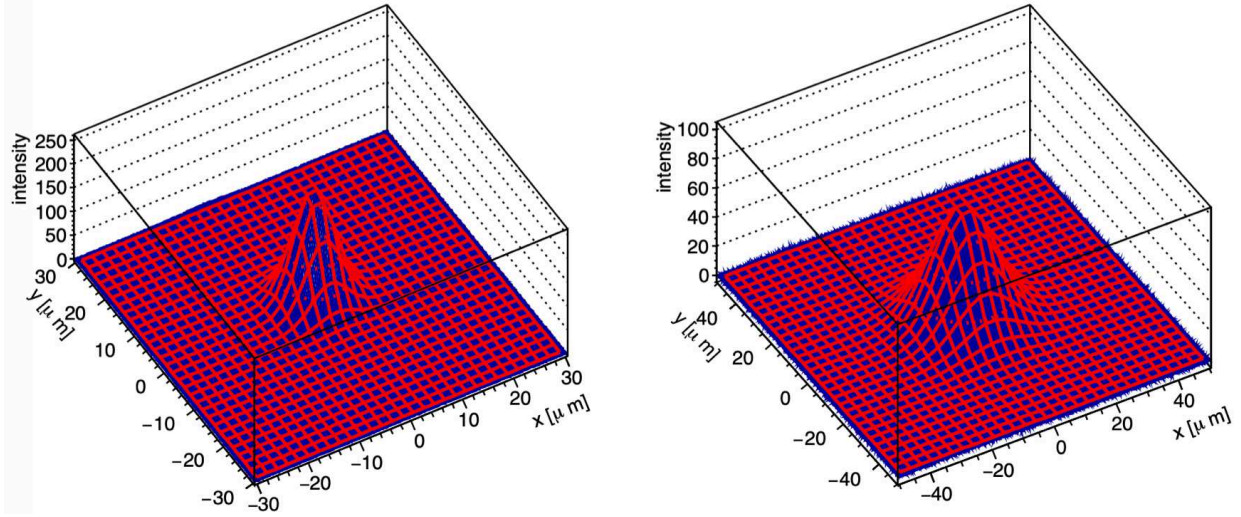


FIG. 10: Fitting of focal-plane intensity profiles with two-dimensional Gaussian distributions constrained by x - y symmetry for creation (left) and inducing (right) beams.

D. Effective energy fraction in Gaussian beams

Figure 10 shows the results of fitting the focal-plane intensity profiles of the creation and inducing beams with two-dimensional Gaussian distributions constrained by x - y symmetry. From the fitting results $\sigma_{xy} = 7$ and $17 \mu\text{m}$ for the creation and inducing lasers, respectively, we evaluated the effective energy fraction contained in the region within $3 \sigma_{xy}$ among the entire intensity profiles, including the peripheral diffraction parts that are assumed not to contribute to stimulated photon-photon scattering.

V. SEARCH RESULT

By combining linearly polarized creation laser pulses and circularly polarized inducing laser pulses, searches for scalar and pseudoscalar resonance states were performed at a vacuum pressure of 2.6×10^{-5} Pa. The arrival-time distributions of photons identified by the peak finder are shown in Fig. 11 for the individual trigger patterns. The area subtended by the two red lines corresponds to the expected signal timing window. The total number of shots in trigger pattern S was $W_S \equiv 2.9993 \times 10^4$.

Figure 12 shows the arrival-time distribution of the number of photons after subtraction between different trigger patterns based on Eq. (18). The total number of signal photons

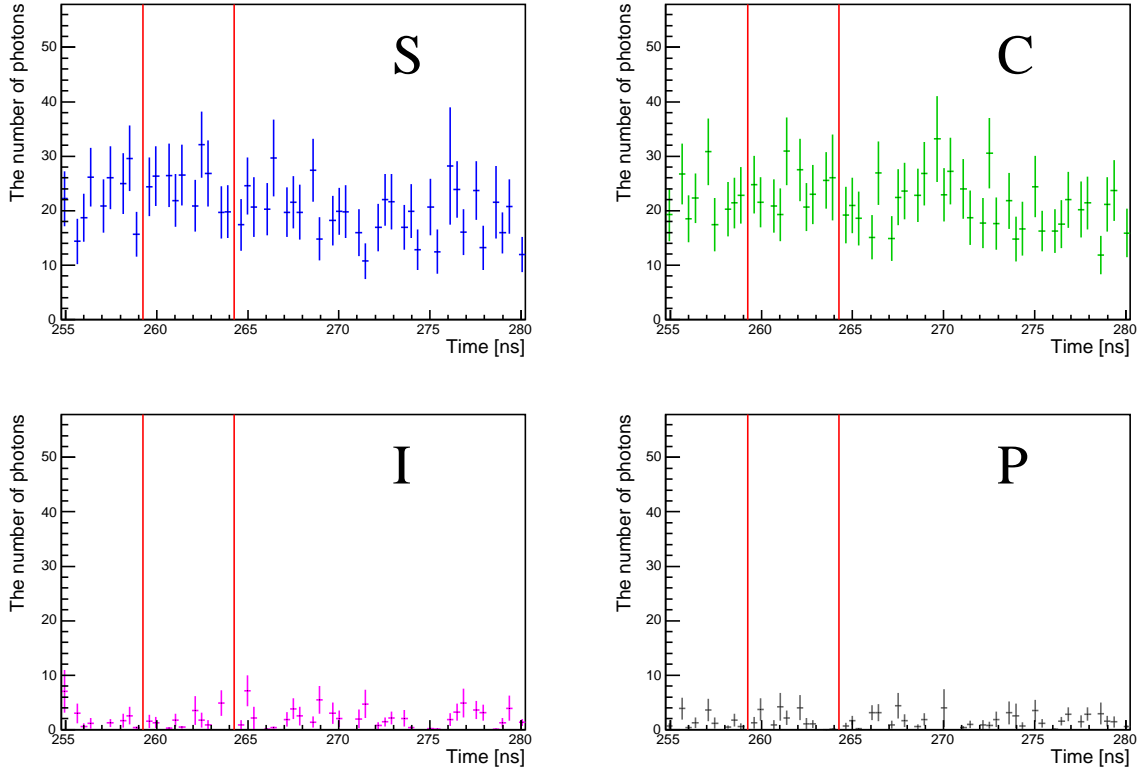


FIG. 11: Arrival-time distributions of detected photons at 2.6×10^{-5} Pa for trigger patterns S, C, I, and P by combining the P-polarization state (creation) and the left-handed circular polarization state (inducing).

within the signal incident timing window was obtained as

$$N_S = 4.9 \pm 22.8(\text{stat.}) \pm 22.8(\text{syst.I}) \pm 3.8(\text{syst.II}) \pm 3.7(\text{syst.III}). \quad (22)$$

Systematic error I was estimated by measuring the root-mean-square of the number of photon-like signals excluding the signal window, corresponding to the baseline uncertainty on the number of photons. Systematic error II reflects time variations of the overlap factors defined in Eq. (21) between the focal spots of the creation and inducing lasers. Note that this equation contains fluctuations of beam energies during a run period as well as the pointing fluctuations. Systematic error III was obtained by changing the threshold value in the peak finder, $V_{th} = (-1.3 \pm 0.1)$ mV, by assuming a uniform distribution from -1.2 to -1.4 mV.

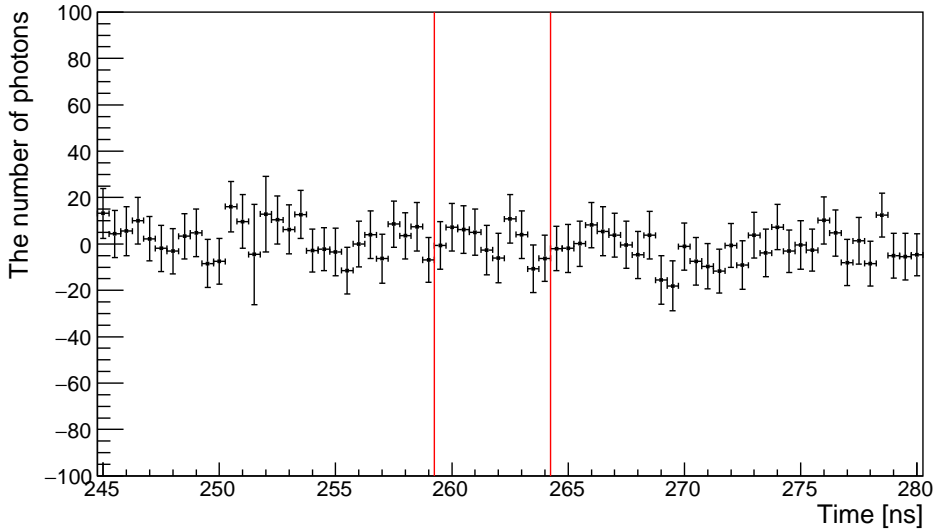


FIG. 12: Arrival-time distribution of number of photons obtained by applying Eq. (18) to the entire timing windows including the signal window enclosed by the two red lines at 2.6×10^{-5} Pa by combining the P-polarization state (creation) and the left-handed circular polarization state (inducing).

VI. UPPER LIMITS ON COUPLING–MASS RELATION FOR ALP EXCHANGES

From the result in (22), we conclude that no signal photons in the quasi-vacuum state were observed based on the total uncertainty. Indeed, this result is also consistent with the expected number of background photons per shot (efficiency-uncorrected) due to residual gases, estimated as

$$N_{gas}/shot = 1.8 \times 10^{-12} \quad \text{photons} \quad (23)$$

by extrapolating to 2.6×10^{-5} Pa with Eq. (19). In addition, for the given total statistics, the expectation value based on the QED photon–photon scattering process, which is the only possible process in the standard model, is negligibly low at $E_{cms} < 1$ eV [23] even though the stimulation effect is taken into account [24]. Therefore, with respect to a null hypothesis following a Gaussian distribution, we provide the upper limits on the coupling–mass relation by assuming scalar and pseudoscalar field exchanges with the experimental parameters in Table I.

We note that the pulse duration of the Nd:YAG laser, τ_{ibeam} , in Table I is not correspond-

ing to that of the Fourier transform limit due to the different scheme to generate pluses from that of Ti:sapphire laser in which time duration close to reaching the Fourier transform limit is obtained. Thus, the effective time duration reaching the Fourier transform limit, τ_i , which can overlap with the creation pulse duration, τ_c , is evaluated from the spectrum linewidth of the Nd:YAG laser. This treatment is consistent with the basic assumption in [18] where the inducing effect is evaluated based on overlapping pulses individually reaching Fourier transform limits. In addition to the effective time durations, by considering the spatially overlapping regions within $3\sigma_{xy}$ focal spots which are consistent with the Gaussian shapes, the effective numbers of photons per pulses, N_c and N_i , were used for the following limit calculations. In this sense, the following results correspond to conservative upper limits, because the effective beam energies stored in pulses are very much reduced.

As for the upper mass range, because of the inclusion of general asymmetric collisions, this search is sensitive to a heavier mass range compared with the symmetric collision range, expressed as

$$m = 2\omega_c \sin \Delta\theta \sim 2\omega_c \frac{d_c}{2f} = 0.21 \text{ eV} \quad (24)$$

based on values in Table I with $\Delta\theta \equiv d/(2f)$ defined by the focal length f and beam diameter d of the creation laser in Fig. 1. Note, however, that this value is merely a reference mass at which the maximum sensitivity is expected.

A confidence level $1 - \alpha$ to exclude a null hypothesis is expressed as

$$1 - \alpha = \frac{1}{\sqrt{2\pi}\sigma} \int_{\mu-\delta}^{\mu+\delta} e^{-(x-\mu)^2/(2\sigma^2)} dx = \text{erf} \left(\frac{\delta}{\sqrt{2}\sigma} \right), \quad (25)$$

where μ is the expected value of an estimator x following a hypothesis, and σ is one standard deviation. In this search, the estimator x corresponds to N_S , and we assign the acceptance-uncorrected uncertainty δN_S from the quadratic sum of all error components in the result (22) as the one standard deviation σ around the mean value $\mu = 0$. In this search, the null hypothesis is produced from fluctuations of the number of photon-like signals following a Gaussian distribution whose expectation value, μ , is zero for the given total number of shots, $W_S = 2.9993 \times 10^4$. This is because N_S is calculated from subtractions between different trigger patterns whose baseline fluctuations, in principle, should follow Gaussian distributions individually. To obtain a confidence level of 95%, $2\alpha = 0.05$ with $\delta = 2.24\sigma$ is used, where a one-sided upper limit by excluding above $x + \delta$ [25] is applied. To evaluate

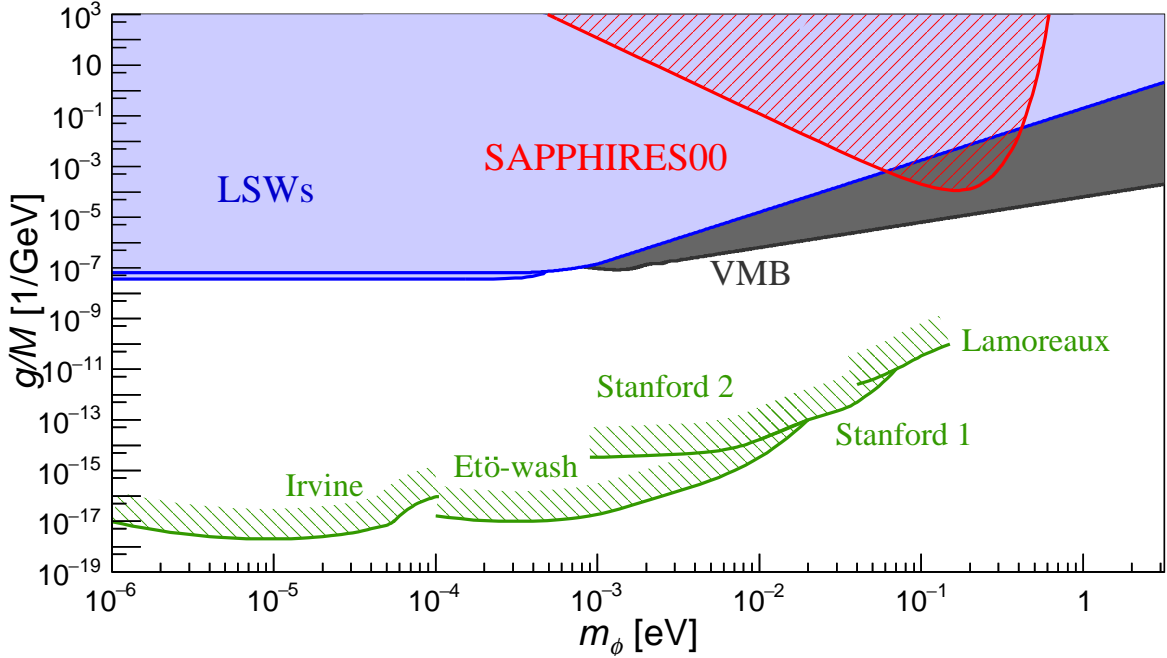


FIG. 13: Upper limits on coupling–mass relation for scalar field (ϕ) exchanges. The red shaded area labeled “SAPPHIRES00” is the region excluded by this work (stimulated resonant scattering). The light-blue area is the region for scalar fields excluded by the “Light Shining through a Wall experiments (LSWs)” (OSQAR [26] and ALPS [27]) with simplification of the sine-function part to unity above 10^{-3} eV for drawing convenience. The gray area is the result from the “Vacuum Magnetic Birefringence (VMB)” experiment (PVLAS [28]). The green shaded areas are regions excluded based on non-Newtonian force searches (“Irvine” [29], “Eto-wash” [30], “Stanford1” [31], “Stanford2” [32]) and on Casimir force measurements (“Lamoreaux” [33]).

the upper limits on the coupling–mass relation, we then solved

$$2.24\delta N_S = \mathcal{Y}_{c+i}(m, g/M; P)t_a r \epsilon \quad (26)$$

numerically based on Eq. (4) with respect to m and g/M for a set of experimental parameters P in Table I, where $t_a r = W_S = 2.9993 \times 10^4$ and the overall efficiency $\epsilon \equiv \epsilon_{opt}\epsilon_d$ with the optical path acceptance ϵ_{opt} to the p_3 detector position and the single p_3 -photon detection efficiency ϵ_d were used. Figures 13 and 14 show the obtained upper limits on the coupling–mass relations for scalar and pseudoscalar fields, respectively, at a 95% confidence level. Note that based on Eq. (17), we used $\epsilon_{opt} = \epsilon_L$ as the optical path acceptance factor, where

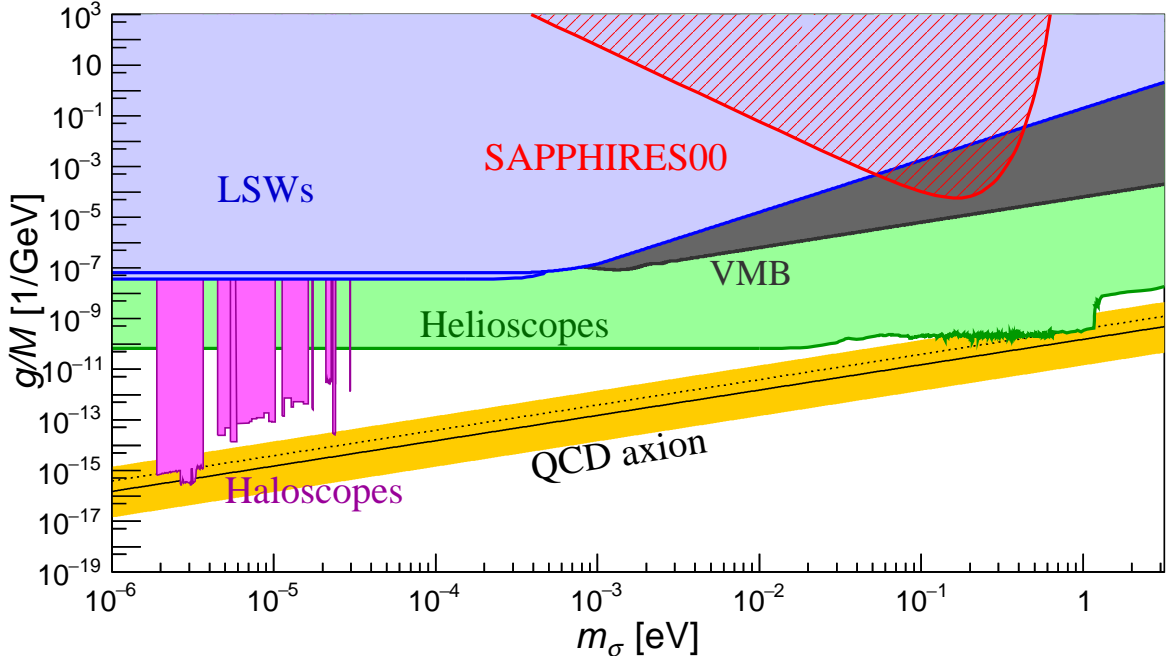


FIG. 14: Upper limits on coupling–mass relation for pseudoscalar fields (σ) exchanges. The red shaded area labeled "SAPPHIRES00" is the region excluded by this work (stimulated resonant scattering). The yellow band shows the coupling–mass relation based on the QCD axion predicted by the KSVZ model [11] with $|E/N - 1.95|$ in the range 0.07–7 with the case of $E/N = 0$ (black dotted line). The case of the DFSZ model [10] with $E/N = 8/3$ is also shown by the black solid line. The light-blue area is the region excluded by LSW experiments (OSQAR [26] and ALPS [27]) with respect to pseudoscalar fields. The gray area is the result from the "Vacuum Magnetic Birefringence (VMB)" experiment (PVLAS [28]). The green area shows upper limits from the "Helioscope" experiment (CAST [34]). The magenta areas are excluded regions from the "Haloscope" experiments (ADMX [35], RBF [36], UF [37], and HAYSTAC [38]).

ϵ_L is the acceptance factor with respect to left-handed circularly polarized photons measured from the IP to the p_3 -detection position. This is because both scalar and pseudoscalar fields can couple only to the same helicity state as that of the inducing field, which is provided as the left-handed state in the searching setup.

TABLE I: Experimental parameters used to numerically calculate the upper limits on the coupling–mass relations. The effective numbers of photons, N_c and N_i , were used for the limit calculations.

Parameter	Value
Central wavelength of creation laser λ_c	816 nm
Relative linewidth of creation laser, $\delta\omega_c / \langle \omega_c \rangle$	1.2×10^{-2}
Duration time of creation laser, τ_c	31 fs (= 36 fs(FWHM)/ $\sqrt{2 \ln 2}$)
Measured creation laser energy per τ_c , E_c	$(100 \pm 5) \mu\text{J}$
Creation energy fraction within $3 \sigma_{xy}$ focal spot, f_c	0.85
Effective creation energy per τ_c within $3 \sigma_{xy}$ focal spot	$E_c f_c = 85 \mu\text{J}$
Effective number of creation photons, N_c	3.5×10^{14} photons
Beam diameter of creation laser beam, d_c	(37.0 ± 0.8) mm
Polarization	linear (P-polarized state)
Central wavelength of inducing laser, λ_i	1064 nm
Relative linewidth of inducing laser, $\delta\omega_i / \langle \omega_i \rangle$	1.0×10^{-4}
Duration time of inducing laser beam, τ_{ibeam}	9 ns
Measured inducing laser energy per τ_{ibeam} , E_i	$(200 \pm 4) \mu\text{J}$
Linewidth-based duration time of inducing laser, $\tau_i/2$	$\hbar/(2\delta\omega_i) = 2.8$ ps
Inducing energy fraction within $3 \sigma_{xy}$ focal spot, f_i	0.87
Effective inducing energy per τ_i within $3 \sigma_{xy}$ focal spot	$E_i(\tau_i/\tau_{ibeam})f_i = 0.11 \mu\text{J}$
Effective number of inducing photons, N_i	5.9×10^{11} photons
Beam diameter of inducing laser beam, d_i	(15.8 ± 0.3) mm
Polarization	circular (left-handed state)
Focal length of off-axis parabolic mirror, f	279.1 mm
Single-photon detection efficiency, ϵ_d	1.4%
Efficiency of optical path from IP to PMT, ϵ_L	33%
Total number of shots in trigger pattern S, W_S	2.9993×10^4 shots
δN_S	32.7

VII. CONCLUSIONS

By combining linearly polarized creation laser pulses and circularly polarized inducing laser pulses, we have searched for scalar and pseudoscalar fields via stimulated resonant scattering by focusing two-color pulsed lasers: 0.10 mJ/31 fs at 816 nm and 0.20 mJ/9 ns at 1064 nm. The observed number of signal photons in the quasi-vacuum state at 2.6×10^{-5} Pa was $4.9 \pm 22.8(\text{stat.}) \pm 22.8(\text{syst.I}) \pm 3.8(\text{syst.II}) \pm 3.7(\text{syst.III})$. We thus conclude that no significant signal was observed in this search. The expected number of signal photons from the residual gas is sufficiently low based on the upper limit from the measurement of the pressure dependence. Based on the assumption that uncertainties are dominated by systematic fluctuations around the zero expectation value following a Gaussian distribution and the fully asymmetric collisional geometry in quasi-parallel stimulated photon–photon scattering, we provided upper limits on the coupling–mass relations for scalar and pseudoscalar fields at a 95% confidence level in the sub-eV mass range.

ACKNOWLEDGMENTS

K. Homma acknowledges the support of the Collaborative Research Program of the Institute for Chemical Research of Kyoto University (Grant Nos. 2018–83, 2019–72, 2020–85, and 2021–88) and Grants-in-Aid for Scientific Research Nos. 17H02897, 18H04354, 19K21880, and 21H04474 from the Ministry of Education, Culture, Sports, Science and Technology (MEXT) of Japan. The authors in ELI-NP acknowledge the support by Extreme Light Infrastructure Nuclear Physics Phase II, a project co-financed by the Romanian Government and the European Union through the European Regional Development Fund and the Competitiveness Operational Programme (No. 1/07.07.2016, COP, ID 1334).

APPENDIX

In order to configure for the actual experimental condition where two beam diameters are different, we replace \mathcal{D}_I in Eq.(A.84) of [18] prepared for the application to the common diameter case between creation (subscript c) and inducing (subscript i) beams with the following factor \mathcal{D}_{c+i} by taking the diameter difference into account.

$$\mathcal{D}_{c+i} = \frac{1}{2} \left(\frac{2}{\pi} \right)^{\frac{3}{2}} \frac{1}{c^2} \frac{\tau_i}{\tau_c} \frac{1}{\sqrt{\tau_c^2 + 2\tau_i^2}} \frac{1}{w_{c0}^2 \left(1 - \frac{z_{cR}^2}{z_{iR}^2} \right)} \left[z_{cR} \tan^{-1} \left(\frac{z_{iR}}{z_{cR}} \right) - R_{ci} Z_{ci} \tan^{-1} \left(\frac{z_{iR}}{Z_{ci}} \right) \right] \quad (27)$$

with

$$R_{ci} \equiv \frac{w_{c0}^2 z_{iR}^2 + 2w_{i0}^2 z_{cR}^2}{z_{iR}^2 (w_{c0}^2 + 2w_{i0}^2)} \quad (28)$$

and

$$Z_{ci} \equiv \sqrt{\frac{w_{c0}^2 + 2w_{i0}^2}{\vartheta_{c0}^2 + 2\vartheta_{i0}^2}} \quad (29)$$

using beam diameters d_k , beam waists w_{k0} , and Rayleigh lengths z_{kR} for $k = c, i$ defined as

$$\vartheta_{k0} = \tan^{-1} \left(\frac{d_k}{2f} \right), \quad (30)$$

$$w_{k0} = \frac{\lambda_k}{\pi \vartheta_{k0}}, \quad (31)$$

$$z_{kR} = \frac{\pi w_{k0}^2}{\lambda_k}. \quad (32)$$

We note that \mathcal{D}_{c+i} is obtained by integrating the spatiotemporal overlapping factor in Eq.(5) over the Rayleigh length of the inducing laser which is longer than that of the creation laser in the experimental setup.

-
- [1] Y. Nambu, Phys. Rev. Lett **4**, 380 (1960); J. Goldstone, Nuovo Cim. **19**, 154 (1961).
[2] R. D. Peccei and H. R. Quinn, Phys. Rev. Lett **38**, 1440 (1977); S. Weinberg, Phys. Rev. Lett **40**, 223 (1978); F. Wilczek, Phys. Rev. Lett **40**, 271 (1978); J. E. Kim, Phys. Rev. Lett. **43**, 103 (1979); M. A. Shifman, A. I. Vainshtein and V. I. Zakharov, Nucl. Phys. B **166**, 493 (1980).
[3] Y. Fujii and K. Maeda, *The Scalar-Tensor Theory of Gravitation* Cambridge Univ. Press (2003).

- [4] R. Daido, F. Takahashi and W. Yin, arXiv:1702.03284 [hep-ph].
- [5] A. Arvanitaki, S. Dimopoulos, S. Dubovsky, N. Kaloper, and J. March-Russell, *Phys. Rev. D* **81**, 123530 (2010); B. S. Acharya, K. Bobkov, and P. Kumar, *J. High Energy Phys.* **11**, 105 (2010); M. Cicoli, M. Goodsell, and A. Ringwald, *J. High Energy Phys.* **10**, 146 (2012).
- [6] John Preskill, Mark B. Wise, Frank Wilczek, *Phys. Lett. B*120, 127 (1983).
- [7] L.F. Abbott, P. Sikivie, *Phys. Lett. B*120 133 (1983).
- [8] Michael Dine, Willy Fischler, *Phys. Lett. B*120, 137 (1983).
- [9] E. Aprile et al., *Phys. Rev. D* **102**, 072004 (2020).
- [10] M. Dine, W. Fischler, and M. Srednicki, *Phys. Lett. B*104, 199 (1981); A. Zhitnitskii, *Sov. J. Nucl. Phys.* 31, 260 (1980).
- [11] J. E. Kim, *Phys. Rev. Lett.* 43, 103 (1979); M. Shifman, A. Vainshtein, and V. Zakharov, *Nucl. Phys. B*166, 493 (1980).
- [12] M. M. Bertolami, B. Melendez, L. Althaus, and J. Isern, *J. Cosmol. Astropart. Phys.* 10 (2014) 069.
- [13] A. Ayala, I. Domínguez, M. Giannotti, A. Mirizzi, and O. Straniero, *Phys. Rev. Lett.* 113, 191302 (2014).
- [14] N. Viaux, M. Catelan, P. B. Stetson, G. G. Raffelt, J. Redondo, A. A. R. Valcarce, and A. Weiss, *Phys. Rev. Lett.* 111, 231301 (2013).
- [15] M. Giannotti, I. G. Irastorza, J. Redondo, A. Ringwald, and K. Saikawa, *J. Cosmol. Astropart. Phys.* 10 (2017) 010.
- [16] L. Di Luzio, M. Giannotti, E. Nardi, and L. Visinelli, *Phys. Rep.* 870, 1 (2020).
- [17] Y. Fujii and K. Homma, *Prog. Theor. Phys* **126**, 531 (2011); *Prog. Theor. Exp. Phys.* 089203 (2014) [erratum].
- [18] Kensuke Homma and Yuri Kirita, *JHEP* 09 (2020) 095.
- [19] K. Homma, T. Hasebe, and K. Kume, *Prog. Theor. Exp. Phys.* 083C01 (2014).
- [20] T. Hasebe, K. Homma, Y. Nakamiya, K. Matsuura, K. Otani, M. Hashida, S. Inoue, S. Sakabe, *Prog. Theor. Exp. Phys.* 073C01 (2015).
- [21] Akihide Nobuhiro, Yusuke Hirahara, Kensuke Homma, Yuri Kirita, Takaya Ozaki, Yoshihide Nakamiya, Masaki Hashida, Shunsuke Inoue, and Shuji Sakabe, *Prog. Theor. Exp. Phys.* 073C01 (2020).
- [22] S. A. J. Druet and J.-P. E. Taran, *Prog. Quant. Electr.* **7**, 1 (1981).

- [23] K. Homma, K. Matsuura, and K. Nakajima, *Prog. Theor. Exp. Phys.* 083C01 (2014).
- [24] K. Homma and Y. Toyota, *Prog. Theor. Exp. Phys.* 2017, 063C01 (2017).
- [25] See Eq.(36.56) in J. Beringer et al. (Particle Data Group), *Phys. Rev. D* **86**, 010001 (2012).
- [26] R. Ballou et al. (OSQAR), *Phys. Rev. D***92**, 9, 092002 (2015).
- [27] K. Ehret et al. (ALPS), *Phys. Lett. B* **689**, 149 (2010).
- [28] A. Ejlli et al. (PVLAS), *Phys. Rept.* 871, 1 (2020).
- [29] Y. Su et al., *Phys. Rev. D* **50**, 3614 (1994); **51**, 3135 (1995) [erratum].
- [30] E. G. Adelberger et al., *Phys. Rev. Lett.* **98**, 131104 (2007); D. J. Kapner et al., *Phys. Rev. Lett.* **98**, 021101 (2007).
- [31] J. Chiaverini et al., *Phys. Rev. Lett.* **90**, 151101 (2003).
- [32] S. J. Smullin et al., *Phys. Rev. D* **72**, 122001 (2005); **72**, 129901 (2005) [erratum].
- [33] S. K. Lamoreaux, *Phys. Rev. Lett.* **78**, 5 (1997); **81**, 5475 (1998) [erratum].
- [34] K. Zioutas et al. (CAST), *Phys. Rev. Lett.* **94**, 121301 (2005); S. Andriamonje et al. (CAST), *J. Cosmol. Astropart. Phys.* **04**, 010 (2007).; E. Arik et al. (CAST), *J. Cosmol. Astropart. Phys.* **02**, 008 (2009); M. Arik et al. (CAST), *Phys. Rev. Lett.* **107**, 261302 (2011); M. Arik et al. (CAST), *Phys. Rev. Lett.* **112**, 9, 091302 (2014); V. Anastassopoulos et al. (CAST), *Nature Phys.* **13**, 584 (2017).
- [35] S. J. Asztalos et al. (ADMX), *Phys. Rev. D* **69**, 01101 (2004); S. J. Asztalos et al. (ADMX), *Phys. Rev. Lett.* **104**, 041301 (2010); N. Du et al. (ADMX), *Phys. Rev. Lett.* **120**, 151301 (2018); C. Boutan et al. (ADMX), *Phys. Rev. Lett.* **121**, 261302 (2018);
- [36] S. De Panfilis et al., *Phys. Rev. Lett.* **59**, 839 (1987); W. U. Wuensch et al., *Phys. Rev. D* **40**, 3153 (1989).
- [37] C. Hagmann et al., *Phys. Rev. D* **42**, 1297 (1990).
- [38] B. M. Brubaker et al., *Phys. Rev. Lett.* **118**, 6, 061302 (2017); L. Zhong et al. (HAYSTAC), *Phys. Rev. D***97**, 9, 092001 (2018).